RESEARCH ARTICLE

NANO · MICRO small

www.small-journal.com

Probing Atomic-Scale Fracture of Grain Boundaries in Low-symmetry 2D Materials

Hui Zhang, Yue Yu, Xinyue Dai, Jinshan Yu, Hua Xu, Shanshan Wang, Feng Ding,* and Jin Zhang**

Grain boundaries (GBs) play a central role in the fracture of polycrystals. However, the complexity of GBs and the difficulty in monitoring the atomic structure evolution during fracture greatly limit the understanding of the GB mechanics. Here, in situ aberration-corrected scanning transmission electron microscopy and density functional theory calculations are combined to investigate the fracture mechanics in low-symmetry, polycrystalline, 2D rhenium disulfide (ReS_2), unveiling the distinctive crack behaviors at different GBs with atomic resolution. Brittle intergranular fracture prefers to rip through the GBs that are parallel to the Re chains of at least one side of the GBs. In contrast, those GBs, which do not align with Re chains on either side of the GBs, are highly resistant to fracture, impeding or deflecting the crack propagation. These results disclose the GB type-dependent mechanical failure of anisotropic 2D polycrystals, providing new ideas for material reinforcement and controllable cutting via GB engineering.

1. Introduction

Grain boundaries (GBs) are key microstructures that govern a material's mechanical properties, including fracture toughness, strength, and crack propagation behaviors. In ductile materials such as metal, GBs commonly impede the migration of dislocations to weaken the plastic flow, which increases strength and hardness yet decreases ductility.[1,2] For brittle materials like ceramics, GBs are thought to perform as the "weak spots" whose strength could be orders of magnitude smaller than the pristine lattice due to a high level of preexisting stress.[3] Therefore, gaining insights into the mechanical properties of GBs is of fundamental importance, which not only pushes the development of "GB engineering" that rationally tailors materials properties by modifying GB's structure, density, and connectivity,[4,5] but also helps answer the question about how the mechanical properties of nanoscale structures are transferred to macroscopic samples.

2D materials provide an ideal platform to investigate the GB fracture mechanics due to their extreme thinness and unambiguous interpretation of the atomic structure.[6–15] Their promising applications in high-end flexible electronic devices,[16,17] electromechanical devices,[18] and reinforcing elements in composites[19] wherein raw materials are often polycrystalline, also necessitate the understanding of fracture mechanics of GBs. Several methods have been developed to unveil the mechanical behaviors of 2D materials. Nanoindentation, which uses the tip in the atomic force microscope

---

H. Zhang, J. S. Yu, S. S. Wang
Science and Technology on Advanced Ceramic
Fibers and Composites Laboratory
College of Aerospace Science and Engineering
National University of Defense Technology
Changsha 410000, P. R. China
E-mail: wangshanshan08@nudt.edu.cn

Y. Yu, S. S. Wang, J. Zhang
Center for Nanochemistry
Beijing Science and Engineering Center for Nanocarbons
Beijing National Laboratory for Molecular Sciences
College of Chemistry and Molecular Engineering
Peking University
Beijing 100871, P. R. China
E-mail: jinzhang@pku.edu.cn

X. Y. Dai, F. Ding
Centre for Multidimensional Carbon Materials
Institute for Basic Science
Ulsan 44919, South Korea

X. Y. Dai
School of Life Sciences
Shanghai University
Shanghai 200444, P. R. China

H. Xu
Key Laboratory of Applied Surface and Colloid
Chemistry Ministry of Education
Shaanxi Key Laboratory for Advanced Energy Devices
Shaanxi Engineering Lab for Advanced Energy Technology
School of Materials Science and Engineering
Shaanxi Normal University
Xi'an 710119, P. R. China

F. Ding
School of Materials Science and Engineering
Ulsan
National Institute of Science and Technology
Ulsan 44919, South Korea
E-mail: f.ding@unist.ac.kr

The ORCID identification number(s) for the author(s) of this article can be found under https://doi.org/10.1002/smll.202102739.

DOI: 10.1002/smll.202102739

(AFM) to apply local stress on a suspended 2D membrane, can quantitatively measure the mechanical parameters, including in-plane elastic modulus and breaking strength.[20–24] Transmission electron microscopy (TEM) with diverse imaging modes and ultrahigh spatial resolution were also applied.[25] Dark-field TEM, serving as a high-throughput technique to map GB distributions, works in conjunction with AFM to accurately impose stress on the GB.[20] Aberration-corrected TEM (AC-TEM) and annular dark-field scanning transmission electron microscopy (ADF-STEM) take advantage of their single-atom resolution and the minor force generated by the electron beam to characterize the fine configuration of crack fronts and to in-situ monitor the dynamic fracture procedure in real time.[26–32] Apart from experimental methods, theoretical calculations such as density functional theory (DFT) calculations and molecular dynamics (MD) simulations have also been widely used to predict the mechanical properties of graphene[33–38] and other low-dimensional materials[27,28,39–42] under extreme strains. DFT calculations can even be applied to elucidate the strain-driven growth mechanism of their GBs.[43]

Although enormous progress has been made, the exact roles of GBs on the material's mechanical properties remain elusive. Nanoindentation tests on graphene done by different groups presented different results. Some indicated GBs to drastically weaken both the fracture strength and the elastic stiffness of graphene,[20,44] while others demonstrated the little negative impact of GBs on mechanical properties of polycrystalline graphene.[21,45] Theoretical calculations reported the superior strength of large-angle tilt GBs compared with low-angle counterparts in graphene due to their enhanced capability to accommodate strains.[46] The ambiguity arises from the diversity and complexity of GB structures, as well as the difficulty in simultaneously viewing GB configuration and its fracture performance down to the atomic level. Moreover, most works were accomplished on high-symmetry crystals (like graphene and MoS_2 with hexagonal lattice), while whether these results can be generalized to low-symmetry ones (like triclinic ReS_2) are unclear.

In this paper, we combine in situ atomic resolution ADF-STEM and DFT calculations to investigate the individual mechanical properties of numerous GBs in a 2D material down to the single-atom level. Polycrystalline ReS_2 monolayers provide an ideal platform, which adopts low lattice symmetry that can construct abundant GB configurations. Brittle intergranular crack by direct cleavage along the grain interfaces is observed, leaving atomically sharp fracture tips without reconstruction and smooth torn edges. Counter to the common idea that regards GBs as the weakness of brittle materials, GBs perform distinctively depending on their detailed configurations. (0°, 60°), $(0°,0°)_R$, and $(0°,120°)_R$ GBs composed of Re—S bonds at the interface are highly susceptible to fracture, while (60°, 120°)R GB consisting of both Re—Re and Re—S bonds exhibits strong resistance to rupture. The experimental observations have been well supported by the calculation of the GB cleavage work function via DFT. These results provide insights into the influence of lattice anisotropy on the fracture mechanics of GBs in low-symmetry 2D materials and may inspire new ideas of GB-mediated engineering of material mechanical properties and applications.

2. Results and Discussion

Monolayer ReS_2 exhibits a distorted octahedral phase (1T' phase) with Re atoms arranged into Re diamond chains.[47–50] It has two principle in-plane axes, denoted as a and b, with nonequivalent lengths and an intersection angle of ≈119° (**Figure 1**). Distinct from the hexagonal 2H phase transition metal dichalcogenides (TMDs) (space group: $P6_3/mmc$), monolayer ReS_2 belongs to the triclinic system with a space group of $P\overline{1}$ that only consists of an inversion center. Since the ADF-STEM image is the 2D projection of the 3D structure, the low-symmetry monolayer ReS_2 not only leads to diversified GBs, but also requires more careful analysis of the GB configuration compared with the high-symmetry 2D materials. As shown in Figure 1A, the middle and right panels demonstrate the atomic models of monolayer ReS_2 after sequentially turning the ReS_2 model on the left panel upside-down (middle panel) and rotating it 180° about an axis perpendicular to the layer (right panel). These two atomic models look the same from the top view with equivalent directions of the Re diamond chains and display as mirror images to the model on the left panel of Figure 1A. However, due to the existence of an inversion center and the incapability of distinguishing the vertical positions of S atoms in different layers from the top view, the side views of the middle and right models are disparate, as indicated by the orange and cyan quadrilaterals. This leads to two potential 3D configurations corresponding to a top-view bi-crystalline model (Figure 1B). One adopts a twin boundary (ii), while the other does not (i). We applied DFT calculations to determine which of these two GB structures is energetically more preferable. Figure S1A (Supporting Information) demonstrates that model (i) well maintains the planar configuration after relaxation, while model (ii) displays prominently out-of-plane deformation and has an energy disadvantage of about 11.82 eV nm^{-1} compared to model (i). For the other GBs, we conducted similar calculations to determine the most thermally stable 3D configuration among all potential structures deduced from the top-view GB image and used the most stable one for the calculation of the fracture mechanics.

We apply the nomenclature of $(\alpha, \beta)_R$ and β_R to define the GB configuration and the structural relation between two neighboring grains, respectively, similar to the previous work.[51] α and β represent the smallest angles rotated from the Re chain direction in a face-down grain to the GB and to the Re chain direction of the adjacent grain anticlockwise, respectively. The letter "R" is used when the two neighboring grains adopt opposite vertical orientations (Figure 1B and Figure S1B, Supporting Information). Figure 1C shows an ADF-STEM image of a bicrystalline region of monolayer ReS_2 with Re diamond chains in different grains marked by pink and blue rhombuses, respectively. The Re atoms at the GB are highlighted in green, which should be named as $(60°, 120°)_R$, and the relation of two grains should be represented as $120°_R$ in light of the nomenclature introduced in this paper. It is noteworthy that the misorientation angles between the GB and the Re chains on both sides of the GB are not exactly 60° and 120° due to the low lattice symmetry of the triclinic ReS_2. However, considering the simplicity of the expression, this nomenclature is applied. In addition, only Re atoms are visible in ADF-STEM images, attributed to

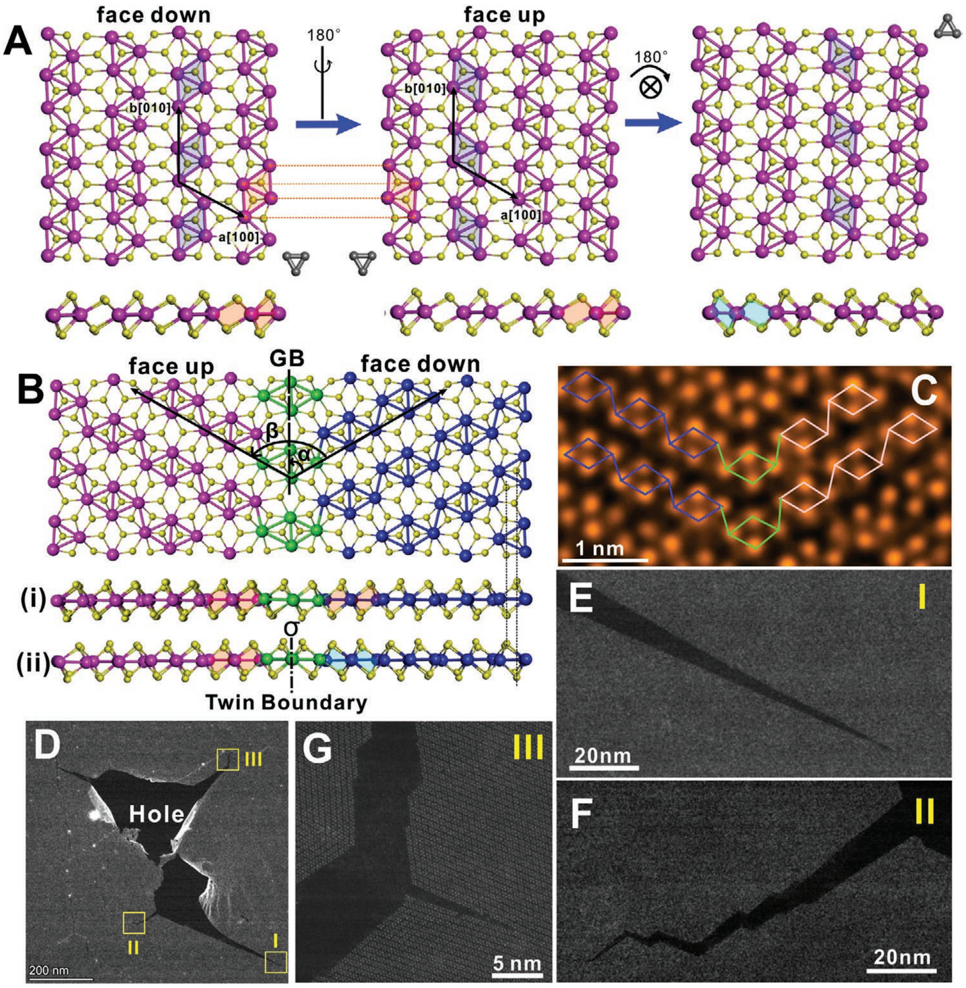

Figure 1. Cracks in polycrystalline monolayer ReS_2. A) Schematic illustrations showing the atomic model of low-symmetry monolayer ReS_2 (left panel) and its configuration changes after sequentially turning the layer upside-down (middle panel) and applying a 180° rotation about an axis normal to the ReS_2 layer (right panel). Both the top and side views of the model are given. The gray triangle beside ReS_2 serves as a reference to facilitate the understanding of different operations to the ReS_2 model. B) Top-view of the atomic model of a ReS_2 bicrystal with a GB and its corresponding two potential side views. C) ADF-STEM image exhibiting a bi-crystalline ReS_2 monolayer region corresponding to the atomic model shown in panel (B). Re diamond chains in distinct grains and the GB are labeled by blue, faded pink, and green, respectively. D) Low-magnification ADF-STEM image showing the crack microstructure after popping the suspended ReS_2 polycrystalline film by the focused electron beam. Three cracks with distinctive features are marked by I, II, and III, respectively. E–G) Zoomed-in ADF-STEM images corresponding to the three yellow boxed regions in panel (D), respectively.

the great variation in the atomic number between Re ($Z = 75$) and S ($Z = 16$) that results in severe contrast difference.

Polycrystalline single-layer ReS_2 was prepared by chemical vapor deposition (CVD) using the method previously reported, which has been confirmed to involve a high density of atomically stitched GBs by the nanoassembly of abundant subgrains.[51] The membrane was transferred onto a holey silicon nitride (SiN_x) TEM grid and got rid of the surface contamination by annealing before ADF-STEM imaging, thus forming intact and freestanding membrane uniformly attached around the hole circumference (Figure S2, Supporting Information). The suspended ReS_2 was subjected to the focused electron beam (e-beam), which was popped by sputtering a hole due to residual stress introduced by the transfer process (Figure 1D).[26] Cracks emanated into surrounding regions and displayed three representative morphologies—a sharp crack tip (Figure 1E), a frequently-deflected fracture trajectory (Figure 1F), and a branched crack (Figure 1G), denoted as I, II, and III, respectively.

Figure 2A is a high-magnification ADF-STEM image showing the fine structure of a sharp crack tip, corresponding to morphology I discussed in Figure 1. The fracture front displays atomic sharpness with two smooth edges having an opening angle of ≈9.1°, indicative of brittle fracture. Interestingly, the ReS_2 monolayer in Figure 2A is constructed by two grains, as highlighted in orange and cyan with the Re diamond chains and three primary lattice directions labeled, respectively. Figure 2B,C are fast Fourier transform (FFT) images of regions marked in orange and cyan in Figure 2A, respectively, where two pairs of brightest reflexes corresponding to (100) and ($\bar{1}00$) crystal planes are labeled, which correspond to the direction of the Re4 diamond chains (b axis) in the real space. The two sets

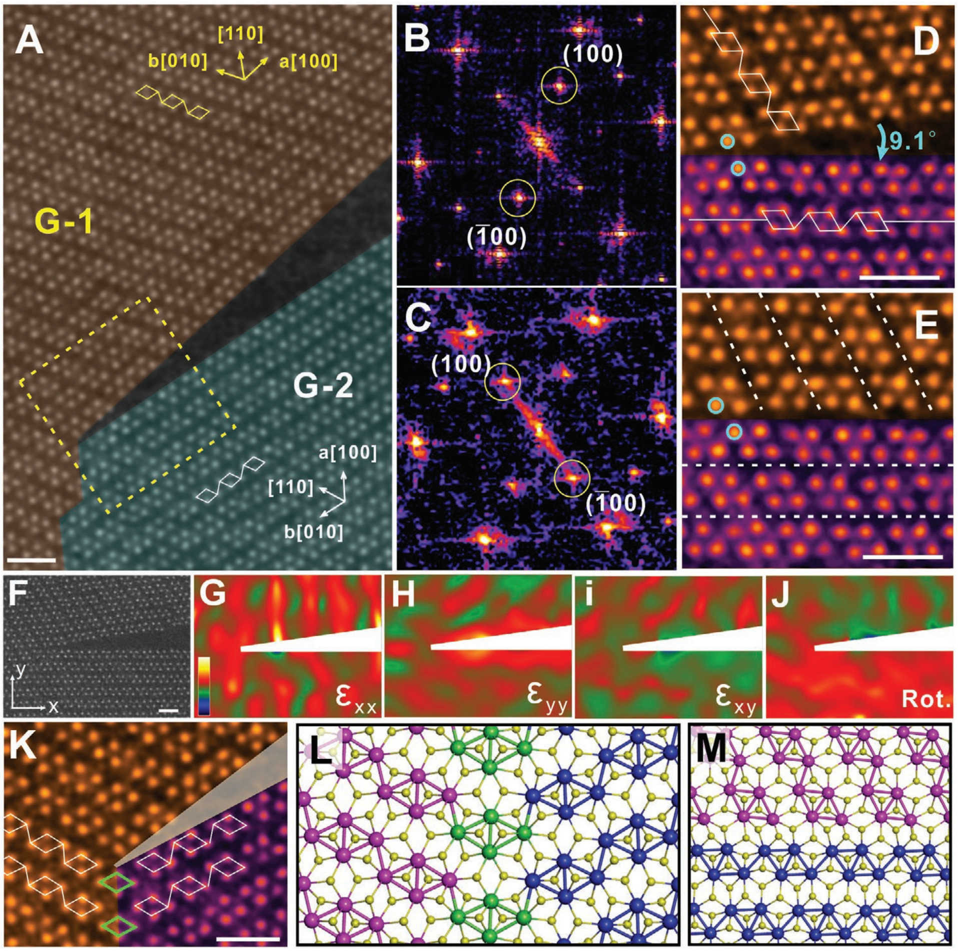

Figure 2. Atomic-resolution ADF-STEM imaging of intergranular crack and the fracture tip. A) ADF-STEM image showing an atomically sharp crack tip (morphology I). Different grains are colored in orange and cyan, respectively, with labels depicting the primary lattice directions and the alignment of Re chains. Scale bar: 1nm. B,C) FFT images corresponding to the lattice highlighted in orange and cyan in panel (A), respectively. D) Zoomed-in ADF-STEM image of the yellow boxed-region in panel (A). Two grains are rendered by orange and fire false-color LUT, respectively. E) Reconstructed ADF-STEM image with the crack eliminated by rotating the upper grain clockwise. Atoms marked by cyan circles in panels (D) and (E) are used as references. White dashed lines highlight the orientations of *b* axes in two grains. F–J) Strain analysis of the crack front. The ADF-STEM image of the crack tip is rotated to be horizontal (panel F) and strain components of ε_{xx}, ε_{yy}, ε_{xy}, and rotation (panels G–J) are extracted by geometric phase analysis from the image. Color bar ranges from -0.5 to 0.5. Scale bar: 1 nm. K) Zoomed-in ADF-STEM image showing the lattice structure below the crack tip, in which a (60°, 120°)$_R$ GB exists. L) Atomic model of the (60°, 120°)$_R$ GB. Re atoms in the face-up and face-down grains are colored in pink and blue, respectively. Re atoms locating at the GB are highlighted in green. M) Atomic model of the (0°, 120°)$_R$ GB corresponding to the ADF-STEM image in panel (E).

of reflexes have disparate orientations, indicating that these two regions on the two sides of the crack in Figure 2A belong to different grains. Combining the information from both the real and reciprocal spaces, the relationship between two adjacent grains can be determined as 120°$_R$, indicating that two grains have opposite vertical directions with a misorientation angle of 120°. It is noteworthy that the fracture proceeded along one GB, generating an intergranular crack, and was stopped in front of another GB, whose orientation is ≈120° by the crack direction. Figure 2D is the zoomed-in image of the yellow boxed-region in Figure 2A with Re atoms of two different grains rendered by orange and fire false colors, respectively, to improve the visual contrast. To unveil the GB configuration that is susceptible to fracture, we rotated the top grain 9.1° clockwise to eliminate the crack, as indicated by the cyan arrow in Figure 2D, thus restoring the GB (Figure 2E). The corresponding atomic model of this GB was shown in Figure 2M, which is an asymmetric tilt GB with an expression of (0°, 120°)$_R$. Two adjacent grains are atomically stitched by generating a series of Re—S bonds. No Re—Re bond reconstruction is involved in the formation of the (0°, 120°)$_R$ GB. The crack rips through it by unzipping the Re—S bonds directly, leaving edges aligning along the crystal directions of [100] (*a* axis) and [010] (*b* axis), respectively. Figure 2F–J evaluates the strain fields around the crack tip using geometric phase analysis (GPA) of the ADF-STEM image. No tension-compression dipoles are identified from the strain profile at the crack front, indicating the absence of lattice reconstruction,[26] thus verifying the brittle behavior of the intergranular fracture in polycrystalline ReS_2 again. Figure 2K magnifies the region of the GB that is resistant to crack, consisting of a string of fourfold

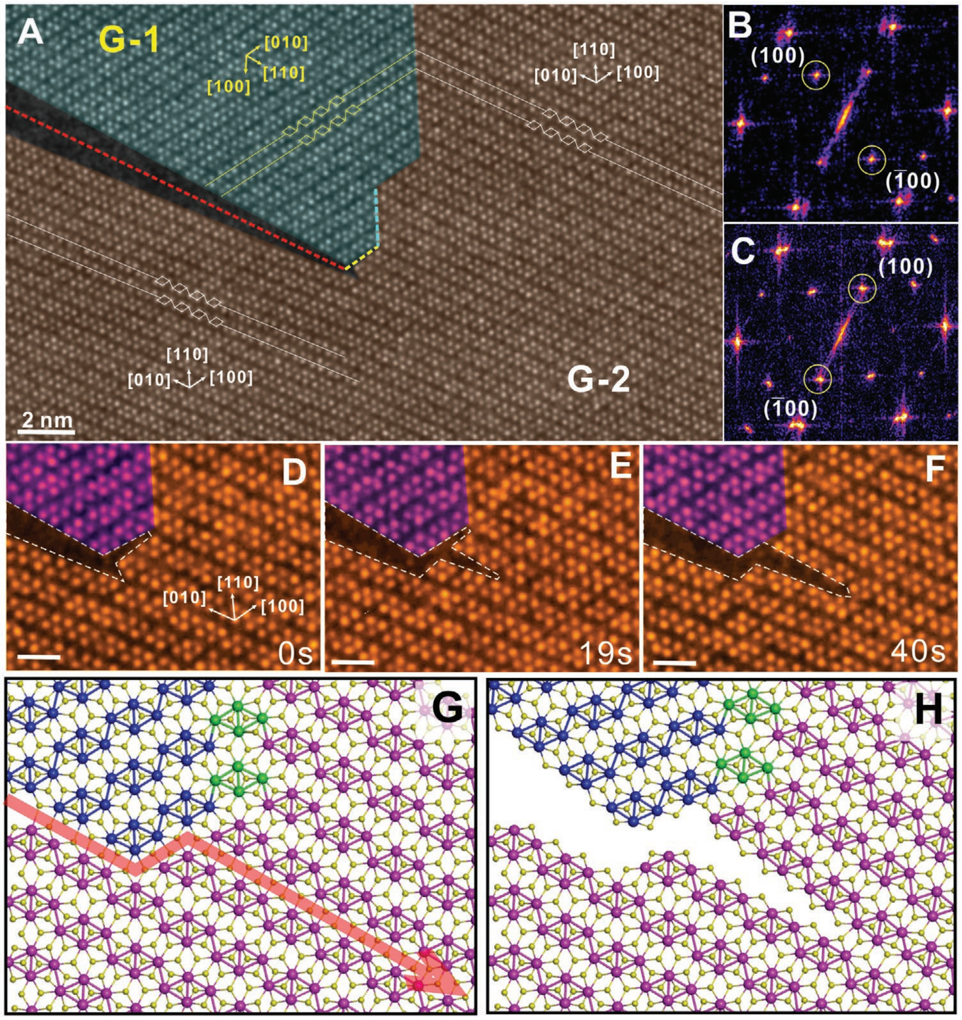

Figure 3. In situ observation of the crack propagation around the GBs. A) ADF-STEM image showing another example of an atomically sharp crack tip in the intergranular fracture. B,C) FFT images corresponding to the cyan and orange regions in panel (A), respectively. D–F) Time series of ADF-STEM images showing dynamics of the crack propagation at the GB. Scale bar: 1 nm. G,H) Atomic models showing the structure of the bicrystalline ReS_2 area before and after the crack rips through. The red arrow in panel (G) indicates the fracture trajectory.

Re rings with slight deformation aligned at the interface to link two neighboring grains, as marked by green rhombuses. The corresponding atomic model is displayed in Figure 2L with an expression of $(60°, 120°)_R$, showing atom-to-atom registry between adjoining grain at the boundary. Figure 2 reveals that GBs in different configurations play distinct roles in the brittle fracture. Some perform as preferential crack propagation sites, while others may impede the advance of fracture. It might derive from the strength variation between Re—S bond and Re—Re bond, as well as the alignment relation between the grains and the GBs influences the GB mechanical properties.

Figure 3 is another example showing an atomically sharp crack tip formed by the intergranular fracture and in-situ monitoring the crack path selection around the junction area of different GBs during fracture propagation. Figure 3A is a medium-magnification ADF-STEM image displaying a crack progressing through a bicrystalline region. Two grains are marked in orange and cyan, respectively, with their corresponding FFT images shown in Figure 3B,C. The relationship between two grains can be defined as $120°_R$, consistent with that in Figure 2. Three GBs are present, expressed as $(120°,120°)_R$, $(0°, 120°)_R$, and $(60°, 120°)_R$, as marked by red, yellow and cyan dashed lines in Figure 3A, respectively. Due to the symmetry of ReS_2, the $(120°,120°)_R$ GB and the $(0°, 120°)_R$ GB are equivalent (Figure S3, Supporting Information). The crack ripped through the bicrystalline area along the $(120°,120°)_R$ GB and stopped at the junction of the $(120°,120°)_R$ and $(0°, 120°)_R$ GBs. Continued imaging of the crack front region triggered low crack advance due to the minor stress generated by the e-beam.[26] Figure 3D–F are time series of zoomed-in ADF-STEM images showing how different GBs influenced the crack trajectory. The crack tip first branched into two directions at the GB junction. One subcrack deflected from the direction of the main crack and went along the $(0°, 120°)_R$ GB, while the other subcrack moved straightforward and advanced to the single-crystalline region along b axis (i.e., lattice direction of [010]), as indicated by dashed white lines in

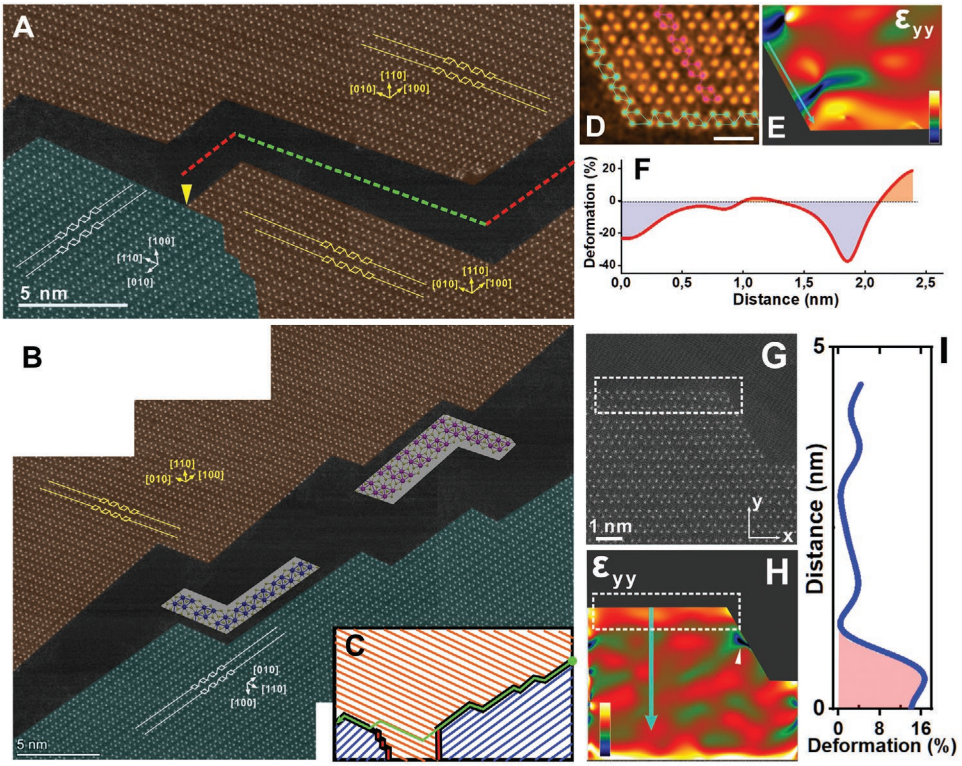

Figure 4. Fracture deflections along GBs. A,B) ADF-STEM images showing a crack path with frequent deflections corresponding to Figure 1F (morphology II). The atomic models of some typical edges are given beside the experimental images in panel (B). C) Schematic illustration showing the grain distribution and the crack trajectory in the polycrystalline region. Blue and orange lines represent the direction of *b* axis in different grains, while the black lines indicate GBs. The green line represents the fracture path. The $(60°, 120°)_R$ GBs that are highly resistant to fracture are highlighted by narrow red lines on top of the thick black lines. D) High-magnification ADF-STEM showing a torn edge with Re diamond chains situating on and a bit farther from the edges marked by cyan and pink lines, respectively. The orange false color has been applied to the ADF-STEM image to enhance the visual effect. Scale bar: 1 nm. E) 2D strain map of ε_{yy} based on the GPA analysis of panel (D). The color bar ranges from –0.5 to 0.5. F) Strain profile taken along the cyan arrow on the fracture edge in panel (E). G) ADF-STEM image showing another torn edge. H) 2D strain map of ε_{yy} based on the GPA analysis of panel (G). Color bar: -0.5 to 0.5. I) Strain profile taken along the cyan arrow from the fracture edge to interior in panel (H).

Figure 3D. As the intergranular crack along the $(0°, 120°)_R$ GB approached the junction formed by $(0°, 120°)_R$ and $(60°, 120°)_R$ GBs, it deflected by ≈60° to avoid encountering the $(60°, 120°)_R$ GB, which exhibited high resistance to fracture, as evidenced by Figure 2 (Figure 3E,F). The crack front finally kinked into the single-crystalline area along b axis, forming a zigzag geometry, and the initial subcrack along b axis in Figure 3D was eliminated. Figure 3G,F elucidate the atomic models of the bicrystalline region before and after the crack went through, implying high susceptibility of the $(0°, 120°)_R$ GB to crack and strong resistance of $(60°, 120°)_R$ GB to fracture. The fracture strength of $(60°, 120°)_R$ GB performs even superior to that of the pristine lattice. It is worth noting that the GBs discussed in this paper are naturally formed in the CVD growth process of monolayer ReS_2 rather than induced by the lattice reconstruction due to the strain around the crack tip zone (Figure S4, Supporting Information). Therefore, the fracture geometry and trajectory in the polycrystalline region can reflect the intrinsic mechanical properties of different GBs (Figures S5 and S6, Supporting Information).

Figure 4 shows a frequently deflected fracture path, denoted as morphology II in Figure 1. Figure 4A,B are ADF-STEM images corresponding to the yellow and red boxed regions in Figure S7A (Supporting Information), respectively. They are Montage of several images stitched together to reveal the high-resolution panorama of the crack trajectory in a large area, showing several deflections and a long-range atomic sharpness of torn edges. The crack was seen to propagate along the low-indexed crystal directions in the pristine lattice and along several GBs. No transgranular fracture was observed. In the single crystalline area, it ripped through *a* and *b* axes, as indicated by red and green dashed lines in Figure 4A, respectively, both leaving smooth edges, verifying the brittle cleavage. In the polycrystalline region, the crack primarily proceeded along the $(0°,120°)_R$ and $(120°, 120°)_R$ GBs, which are isovalent configurations, agreeing well with the phenomena discussed in Figures 2 and 3. Deflections took place mainly due to the terraced geometry of the GBs (Figure 4B). We also witnessed the fracture deflection when a crack tip propagating in a pristine region encountered a $(120°, 120°)_R$ GB, indicative of the yellow arrow in Figure 4A. Although there remains a tiny region between the yellow and red boxes in Figure S7A (Supporting Information) that was not directly captured by ADF-STEM images, we can approximately infer the GB patterns and the crack trajectory in this polycrystalline area based on the information offered by Figure 4A,B (Figure 4C). Brittle intergranular cracks along the (0°,120°)$_R$ and (120°, 120°)$_R$ GBs were the primary fracture modes in these 2D nanoscale patchworks. To avoid meeting with the (60°, 120°)$_R$ GB, which acts as an obstacle to rupture, the crack front propagated into a single-crystalline region following the lattice directions of [010] and [100] in a short period. However, it quickly found another fragile GB nearby to follow, which could be motivated by the least energy consumption principle. Figure 4D is a high-magnification ADF-STEM image showing the typical structure of the torn edges (Figure S7B, Supporting Information). It was found that the outermost Re diamond chains appear to suffer more severe lattice deformation compared with those locating a bit farther from the edges, as indicated by the cyan and pink quadrilaterals (Figure 4D, Figure S7C, Supporting Information). The 2D strain map of ε_{yy} in light of the GPA analysis of Figure 4D displays tension-compression dipoles arranged alternatively along the left edge, which is also supported by the qualitative analysis by taking the strain profile along the cyan arrow (Figure 4E,F). Another fracture edge locating on the opposite side (Figure 4G, Figure S7B, Supporting Information) also exhibited pronounced lattice distortion on the edges, as manifested by the white boxed region in the strain map of ε_{yy} (Figure 4H). Figure 4I shows the deformation level along the cyan arrow in Figure 4H, in which the lattice on the horizontal torn edge displays elongation of ≈20% in the vertical direction compared to the bulk region (Figure S8, Supporting Information). The stretching or shrinkage of the edge lattice in the x–y plane may either arise from the bond length variation between edge atoms owing to their unsaturated coordination compared with bulk or originate from an out-of-plane distortion due to increased freedom of edges, which alters the projected atomic distance.

When a crack propagated through a polycrystalline region that was constructed by intricate patchworks of grains, the fracture path was observed to branch into several directions, since the GBs that are susceptible to rupture are multiple. As shown in **Figure 5**A, five grains were resolved and colored in cyan, red, yellow, orange, and green, respectively, with their *a* and *b* axes labeled. The main crack entered from the bottom left of the image and then divided into two directions, as pointed out by the white lines, respectively. To accurately resolve the interface configurations that the crack ripped through, we restored the original pattern of this polycrystalline area by fitting different pieces of ReS_2 lattice back together based on the complementarity of torn edges in brittle fracture, similar as solving a jigsaw puzzle (Figure 5B, Figure S9, Supporting Information). Re diamond chains in disparate grains situating along the crack trajectory are marked. It can be clearly seen that the crack still preferred to tear along GBs, generating intergranular fracture in this polycrystalline area composed of dense grains. Three main GB structures represented by red, yellow, and green dashed lines in Figure 5B can be unambiguously resolved, named as (0°, 60°), (0°, 0°)$_R$, and (0°, 120°)$_R$. The first two GBs are not encountered in the previous discussion. The GB shown in Figure 5C are constructed by two grains that have the same vertical direction but adopt an in plane twist angle, while the GB in Figure 5D is generated by two grains having the opposite vertical direction but showing the parallel orientation of the Re chains. The panorama of the atomic structure around the crack bifurcation point is displayed in Figure 5F with the 3D perspective view shown in Figure 5G. Similar to the scenarios discussed in the previous examples, the intergranular fracture is prone to split the GBs that are interlinked by Re—S bonds and avoid rupturing GBs that necessitate to cleave Re—Re bonds like (60°,120°)$_R$. To sum up, we measured four different samples. 28 GBs were imaged to crack. Among them, cracks along the (0°, 120°)$_R$ GB were the most commonly observed, whose number is 25. Fracture along the (0°,60°) GB and the (0°,0°)$_R$ GB were less observed, whose numbers are 2 and 1, respectively. The reason why the intergranular fracture along the (0°, 120°)$_R$ GB was more frequently detected may come from the quantity difference between different GBs in our specimen. Since the intergranular fracture along the (0°,60°) GB and the (0°,0°)$_R$ GB was relatively less observed compared with that along the (0°, 120°)$_R$ GB, we introduced DFT calculation in **Figure 6** to replenish the analysis of their fracture mechanics from a theoretical perspective. Six (60°, 120°)$_R$ GBs were imaged to prohibit the fracture propagation. Therefore, our experimental results are reproducible (Figures S10 and S11, Supporting Information).

GBs can also trigger instability in the crack propagation, inducing perturbation of the fracture path that decreases the smoothness of the torn edges and introduces residual chains. Figure 5H is the zoomed-in ADF-STEM image showing the atomic configuration of one crack branch corresponding to the yellow boxed-region in Figure 5A. The crack front initially moved along the (0°,0°)$_R$ GB. When it approached a kink of the GB (yellow arrow), the crack did not deflect upward to continue following the (0°,0°)$_R$ GB but rather propagated straightforward along the *b* axis into the pristine lattice. However, the interplay between the fracture front and the GB kink induced complicated lattice reconstruction in this region, leaving a Re single-atom chain (cyan arrow) and causing local edge irregularity. The reason why the fracture path here did not strictly follow the geometry of the (0°,0°)$_R$ GB may originate from the energy balance between the path deflection and the strength difference of the pristine lattice and the GB. When the fracture strength discrepancy between the *b* axis of the pristine ReS_2 and the (0°,0°)$_R$ GB is small, a deflection of the crack path may be energetically unfavorable compared with moving straight into the pristine lattice.

DFT calculations were conducted to give theoretical insights into the fracture mechanics of different GBs in anisotropic ReS_2 monolayers. Figure 6A–E are the optimized atomic models of a perfect single-layer ReS_2 and the ReS_2 with diverse GBs imaged in the STEM experiments. We first calculated the stress-strain curves of corresponding GBs by applying an in-plane external loading normal to the GB orientations (Figure 6F). Previous work has proved that both the ultimate tensile strength and the critical strain are the lowest in a perfect ReS_2 when the stress is exerted perpendicular to the orientation of the Re diamond chain (*b* axis), thus inducing cleaved edges parallel to this direction. In contrast, the crack perpendicular to the Re chain orientation is the hardest to take place due to the strong Re—Re covalent bonding that results in high breakage resistance.[52] Therefore, we used the mechanical properties along and perpendicular to the Re chains in a perfect ReS_2 monolayer, denoted as || and ⊥ Re-chain, respectively, as two references to

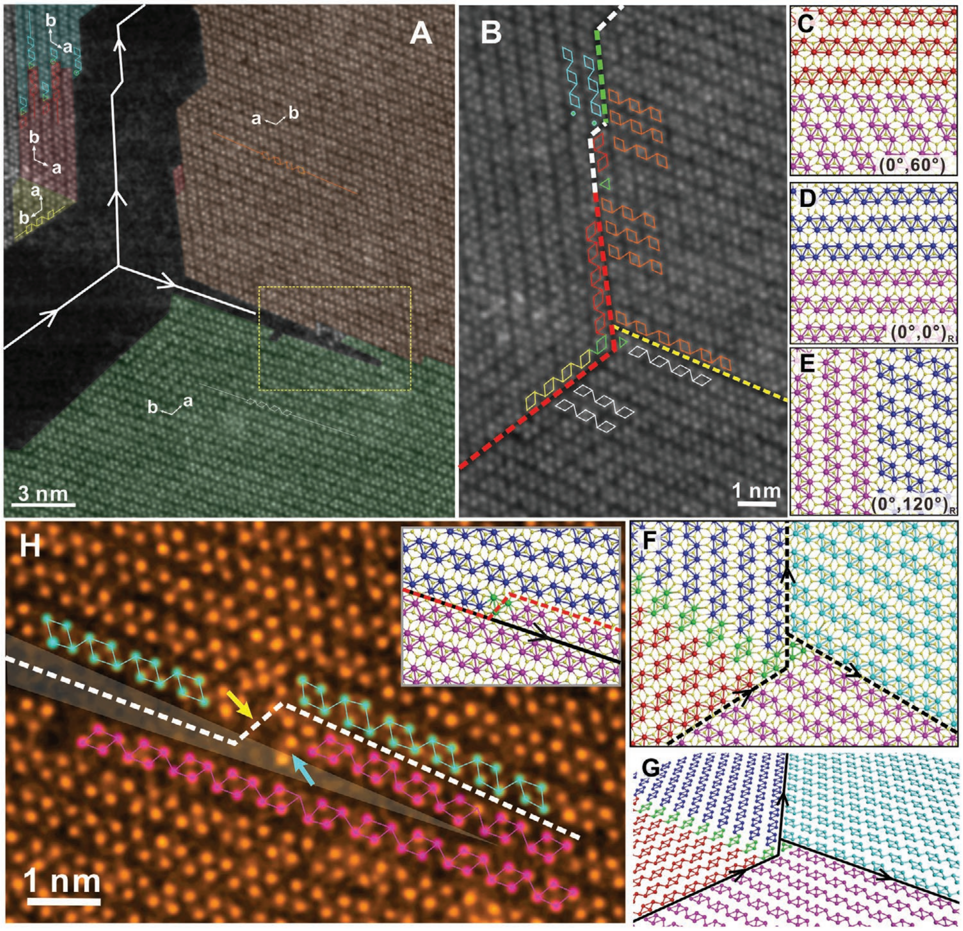

Figure 5. Atomic-resolution ADF-STEM imaging of the branched crack. A) ADF-STEM image of the branched crack (morphology III). The intricate 2D nanoscale patchworks of different grains are represented in cyan, red, yellow, orange, and green, respectively. White lines indicate the crack path and directions. B) Restored ADF-STEM image showing this region before the crack passed through by fitting different parts of lattice together based on the complementary morphology of the fracture edges. Re diamond chains close to the fracture path in different grains are labeled in disparate colors. The crack trajectories are marked by dashed lines. Different line colors represent different GB configurations, and the interface structures in red, yellow, and green are discussed in detail due to their unambiguous atomic arrangement. C–E) Atomic models showing the GB structures corresponding to the interfaces marked by red, yellow, and green dashed lines in panel (B), respectively. Grains with Re atoms colored in pink and blue indicate that two grains have reversed vertical directions, while grains having Re atoms colored in pink and red mean that neighboring grains adopt the same vertical direction. F) Atomic model (projected view) showing the polycrystalline structure around the crack bifurcation point corresponding to panel (B). The fracture paths are labeled by the black dashed lines. G) 3D perspective view of the atomic model in panel (F) with S atoms hidden. H) High-magnification ADF-STEM image showing the right crack branch corresponding to the yellow boxed region in panel (A). Re diamond chains in two grains around the crack path are represented by cyan and pink spheres, respectively. The GB is labeled by the white dashed line. The residual chain between the fracture gap due to the fracture instability at the GB is highlighted by the cyan arrow. Inset is the atomic model showing the lattice structure of this region before the crack. The black solid line indicates the crack path, while the red dashed line represents the GB.

evaluate the mechanical properties of different GBs in ReS_2 observed in our experimental studies. Figure 6F shows that the $(60°, 120°)_R$ GB has the highest ultimate strength among all the atomic configurations calculated, yielding 20.17 GPa, which is not only prominently superior to the other three kinds of GBs but also surpasses the strongest direction of a perfect ReS_2. On the contrary, the ultimate strengths of the $(0°, 120°)_R$, $(0°, 0°)_R$ and (0°,60°) GBs are 14.89, 15.88 and 14.61 GPa, respectively, all of which are inferior to the weakest strength in a perfect ReS_2.

Figure 6G displays the cleavage work functions, a parameter to evaluate the fracture toughness, of the corresponding GBs by integrating the areas beneath their stress-strain curves. Similar to the scenarios in the ultimate strength calculation, the $(60°, 120°)_R$ GB shows the highest cleavage work function (186.80×10^9 J m^{-3}) among all four types of GBs, which also exceeds that along *b* axis in a perfect ReS_2 by more than 70%, indicating a large amount of energy required for a crack to grow along this GB. In comparison, the cleavage work functions of $(0°, 120°)_R$, $(0°, 0°)_R$ and (0°,60°) GBs are 96.57×10^9 J m^{-3}, 105.07×10^9 J m^{-3} and 94.05×10^9 J m^{-3} respectively, all of which are lower than that along the Re chains (107.21×10^9 J m^{-3}). Ultimate tensile strength as a function of the cleavage work function is shown in Figure 6I, indicating a positive relationship between these two parameters. These calculated results demonstrate that both strength and toughness of the $(60°, 120°)_R$ GB are superior to the pristine monolayer ReS_2 if the lattice is pulled apart

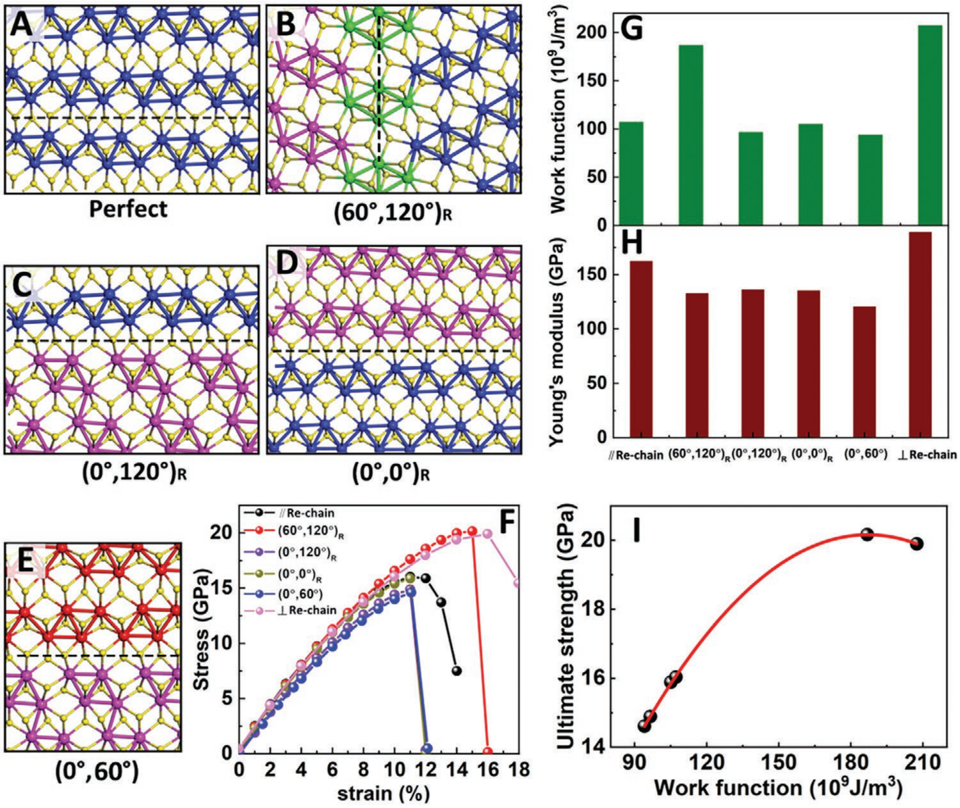

Figure 6. Mechanical properties of different GBs in monolayer ReS_2 calculated by DFT method. Atomic structures of perfect ReS_2 A) and ReS_2 with different types of GBs: B) with a $(60°,120°)_R$ GB, C) with a $(0°,120°)_R$ GB, D) with a $(0°,0°)_R$ GB, and E) with a (0°,60°) GB. F) The calculated stress-strain curves of a perfect ReS_2 and those with different types of GBs when the external stress is applied perpendicular to the GB direction. G) The calculated cleavage work functions of the corresponding atomic structures, which are the areas beneath the stress–strain curves. The signs of "∥" and "⊥ Re-chain" indicate that the fracture orientation is parallel with or perpendicular to the Re diamond chain in a perfect ReS_2 monolayer, respectively. H) The calculated Young's modulus of the corresponding atomic structures. I) Ultimate tensile strength as a function of the cleavage work function.

along the Re chains, which well explained why fracture can be impeded or deflected by this type of GB. In contrast, $(0°, 120°)_R$, $(0°, 0°)_R$, and (0°, 60°) GBs deteriorate the mechanical properties of the pristine ReS_2, performing as the "weak spots" of the lattice and thus attracting intergranular fracture (Figure S12, Supporting Information).

It is worth noting that the mechanical performance of the GBs in ReS_2 closely correlates with their orientation relationship with the Re chains. If the alignment of the GB is parallel to the Re chains of at least one side of the GB, only Re—S bonds are present at the grain interface and the GB will be highly susceptible to crack. However, if the GB direction does not align with the Re chains of either side of the GB, strong Re—Re bonds will be generated at the interface, thus making the GB highly resistant to rupture. Such an abnormal behavior is closely related to the pronounced anisotropic mechanical properties of ReS_2, which originates from its low lattice symmetry.

We also calculated the Young's modulus for different GBs according to the stress–strain curves, as provided in Figure 6H. It can be concluded that the Young's modulus of the perfect monolayer ReS_2 along the direction which is perpendicular to the direction of Re chain is lower than that along the Re chain direction, i.e., 162.20 versus 188.85 GPa. The Young's modulus of ReS_2 with different GBs are 132.68, 136.06, 135.25, and 120.55 GPa, respectively, all of which are lower than the modulus of a perfect ReS2. The results show that the rigidity of the monolayer ReS_2 with GBs slightly decreases.

3. Conclusion

In summary, our study demonstrates that the effect of GBs on the material mechanical properties is highly structure-dependent and enables us to correlate the configuration of diverse GBs to their specific fracture mechanics at the atomic level. These findings are achieved by conducting in situ ADF-STEM on the ultrathin, low-symmetry, polycrystalline materials, capacitating simultaneous achievement of abundant GBs, the ambiguous atomic interpretation of their structures, and monitoring the crack behavior at different GBs. Brittle intergranular fracture is prone to propagate along some types of GBs but avoids others depending on their alignment relationship with the Re chains and the atomic configurations at the grain interfaces. DFT calculations show that some GBs can simultaneously improve the strength and toughness of the material. The interplay between the GB and the crack occasionally may induce crack propagation instability, resulting in irregular torn edges and residual Re atom chains locally. These results give fundamental insights into the role of different GBs in the material mechanics, providing new paths to material reinforcement (via introducing fracture-resistant GBs) and high-resolution nanopattern manufacture (via programming fracture-susceptible GBs with specific geometry), which have great potential in electronics, optics, microfluids, etc.

4. Experimental Section

CVD Synthesis and Transfer of Monolayer ReS_2: Monolayer ReS_2 was synthesized by a hydrogen-free CVD approach using rhenium trioxide (ReO_3, 99.9%, Sigma-Aldrich) and sulfur (S, 99.5%, Sigma-Aldrich) as precursors.[51,53] Silicon substrate with a layer of oxide films (SiO_2/Si) or mica can be used as the substrate. The crucible containing ReO_3 was located at the furnace center, maintaining the temperature of 600–800 °C for the ReS_2 growth, while S powder was placed upstream of the furnace with heating temperature of ≈200 °C. The reaction lasted for 10 min. The furnace was naturally cooled to room temperature after growth. For the preparation of the STEM sample, a thin film of poly (methyl methacrylate) (PMMA) was initially spin-coated on the ReS_2/SiO_2/Si substrate surface. Subsequently, the sample was gently floated on a 1 mol L^{-1} potassium hydroxide (KOH) solution to etch SiO_2 away. When the PMMA/ReS_2 film detached from the Si substrate, the film was transferred to the deionized water for three times to thoroughly remove residuals left by the etchant. The PMMA/ReS_2 film was scooped up by a holey silicon nitride (SiN_x) TEM grid, dried naturally in the air and baked on the hotplate at 180 °C for 15 minutes. The PMMA scaffold was finally removed by submerging the TEM grid in acetone for 8 h.

Generation of Cracks in Monolayer ReS_2: Three steps were applied to in situ generate cracks of monolayer ReS_2 in the TEM column. First, the monolayer sample was annealed at 300 °C with argon used as the carrier gas before imaging so that hydrocarbon contamination can be partially removed from the specimen surface and a small amount of strain was introduced in the suspended film due to the baking process. Second, a suspended ReS_2 monolayer membrane was chosen which was intact and fully covered a hole of the silicon nitride grid with a diameter of 2 µm. Third, the electron beam was converged under TEM mode. The accelerating voltage was 300 kV with a dose rate of 17000 e per $Å^{-2}$ s^{-1}. After around 30 s, cracks can be generated and some of the cracks were seen to extend hundreds of nanometers to the surrounding regions. There are some key points that severely influence the success of the crack initiation. First, the surface of the sample should be clean. A fresh sample is more suitable than an aged one because the surface contamination can serve as adhesive which prohibits the sample fracture. Second, the suspended membrane should be intact before the crack generation since a broken film hardly stores prestress which is not conducive to the crack growth.

Scanning Transmission Electron Microscopy and Image Processing: ADF-STEM imaging was conducted at room temperature on an aberration-corrected Titan Cubed Themis G2 300 transmission electron microscope. STEM was operated under an accelerating voltage of 300 kV. Dwell time of a single frame was 2 µs per pixel. A pixel size of 0.012 nm px^{-1} with a beam current of 8–10 pA was used for imaging. Conditions were a condenser lens (CL) aperture of 50 µm, convergence semi-angle of 21.3 mrad, and inner acquisition angle of 39–200 mrad. The electron dose applied in the system is approximately two orders of magnitude smaller than those used in the low accelerating voltage STEM systems,[12,54] which partially balanced the irradiation effect from the high accelerating voltage. Therefore, one did not observe obvious damage to the ReS_2 lattice due to the e-beam illumination under this imaging recipe. Images were processed using the ImageJ software. False-color LUTs were applied to grayscale images to improve of the visual effect. A Gaussian blur filter (≈2–4 pixels) was used on high-mag ADF-STEM images for smoothing. Atomic models were constructed using the software of Accelrys Discovery Studio Visualizer. ADF-STEM image simulations based on corresponding atomic models were generated using COMPUTEM software with a proper parameter adjustment according to the imaging conditions.

Calculation Methods: To calculate the mechanical properties of ReS_2 GBs, first-principles calculations were carried out with the Vienna Ab initio Simulation Package (VASP) based on DFT. The exchange-correlation function of generalized gradient approximation (GGA) of Perdew-Burke-Ernzerhof (PBE) was adopted.[55–57] The electronic plane wave interception energy was set to be 550 eV for all the structural optimization. For the atomic relaxations and the calculations of mechanical properties of ReS_2 GBs, k-point meshes of 1 × 3 × 2 for $(60°, 120°)_R$ (32 ReS_2 pairs), 3 × 2 × 3 for (0°, 60°) and $(0°, 120°)_R$ (32 ReS_2 pairs) and 3 × 1 × 2 for $(0°, 0°)_R$ (32 ReS_2 pairs) unit cells were used. As for the comparison of two different $(60°, 120°)_R$ configurations (64 ReS_2 pairs) with and without twin boundaries, the k-points mesh was set as 1 × 3 × 2. The vacuum layer between neighboring ReS_2 layers was set to be larger than 13.5 Å to avoid the interactions between neighboring images. All the structures were relaxed until the energy differences were converged within 10^{-5} eV and the forces of all atoms were less than 0.01 eV $Å^{-1}$.

Supporting Information

Supporting Information is available from the Wiley Online Library or from the author.

Acknowledgements

J.Z. acknowledges financial support from the Ministry of Science and Technology of China (2016YFA0200100 and 2018YFA0703502), the National Natural Science Foundation of China (Grant Nos. 52021006, 51720105003, 21790052, 21974004), the Strategic Priority Research Program of CAS (XDB36030100), and the Beijing National Laboratory for Molecular Sciences (BNLMS-CXTD-202001). S.W. acknowledges support from the National Natural Science Foundation of China (52172032, 21805305), State Administration of Science, Technology and Industry for National Defense (WDZC20195500503), the China Postdoctoral Science Foundation (2020M680231), and National University of Defense Technology (ZK18-01-03, ZZKY-YX-09-01). F.D. and X.D. acknowledge the support of Research Foundation in Institute for Basic Science (IBS-R019-D1), Republic of Korea and usage of the high-performance computing (HPC) system, Simulator. H.X. acknowledges the financial support from the National Natural Science Foundation of China (51972204).

Conflict of Interest

The authors declare no conflict of interest.

Author Contributions

H.Z., Y.Y., and X.D. contributed equally to this work. J.Z. and S.W. initiated the project and generated the experimental protocols. Y.Y. and S.W. fabricated the STEM sample and conducted the ADF-STEM imaging. F.D. and X.D. performed DFT calculations. H.Z., J.Y., and H.X. provided CVD-grown monolayer ReS_2 samples. All authors contributed to the data analysis, manuscript writing and revision of the manuscript.

Data Availability Statement

Research data are not shared.

Keywords

2D materials, atomic scale, density functional theory, fracture mechanics, grain boundaries, low symmetry, scanning transmission electron microscopy

Received: May 10, 2021
Revised: August 24, 2021

---

[1] X. C. Liu, H. W. Zhang, K. Lu, *Science* **2013**, *342*, 337.
[2] R. O. Ritchie, *Nat. Mater.* **2011**, *10*, 817.
[3] G. Sernicola, T. Giovannini, P. Patel, J. R. Kermode, D. S. Balint, T. Ben Britton, F. Giuliani, *Nat. Commun.* **2017**, *8*, 108.
[4] S. Ramtani, *Science* **2013**, *342*, 320.
[5] M. Seita, J. P. Hanson, S. Gradečak, M. J. Demkowicz, *Nat. Commun.* **2015**, *6*, 6164.
[6] A. K. Geim, K. S. Novoselov, *Nat. Mater.* **2007**, *6*, 183.
[7] J. H. Warner, E. R. Margine, M. Mukai, A. W. Robertson, F. Giustino, A. I. Kirkland, *Science* **2012**, *337*, 209.
[8] S. Wang, G.-D. Lee, S. Lee, E. Yoon, J. H. Warner, *ACS Nano* **2016**, *10*, 5419.
[9] A. Hashimoto, K. Suenaga, A. Gloter, K. Urita, S. Iijima, *Nature* **2004**, *430*, 870.
[10] K. Suenaga, M. Koshino, *Nature* **2010**, *468*, 1088.
[11] W. Zhou, X. Zou, S. Najmaei, Z. Liu, Y. Shi, J. Kong, J. Lou, P. M. Ajayan, B. I. Yakobson, J.-C. Idrobo, *Nano Lett.* **2013**, *13*, 2615.
[12] S. Wang, H. Sawada, X. Han, S. Zhou, S. Li, Z. X. Guo, A. I. Kirkland, J. H. Warner, *ACS Nano* **2018**, *12*, 5626.
[13] S. Wang, H. Li, J. Zhang, S. Guo, W. Xu, J. C. Grossman, J. H. Warner, *ACS Nano* **2017**, *11*, 6404.
[14] J. Y. Huang, F. Ding, B. I. Yakobson, P. Lu, L. Qi, J. Li, *Proc. Natl. Acad. Sci. USA* **2009**, *106*, 10103.
[15] S. Wang, Y. Yu, S. Zhang, S. Zhang, H. Xu, X. Zou, J. Zhang, *Matter* **2020**, *3*, 2108.
[16] X. Zhang, J. Grajal, J. L. Vazquez-Roy, U. Radhakrishna, X. Wang, W. Chern, L. Zhou, Y. Lin, P. C. Shen, X. Ji, X. Ling, A. Zubair, Y. Zhang, H. Wang, M. Dubey, J. Kong, M. Dresselhaus, T. Palacios, *Nature* **2019**, *566*, 368.
[17] G.-H. Lee, Y.-J. Yu, X. Cui, N. Petrone, C.-H. Lee, M. S. Choi, D.-Y. Lee, C. Lee, W. J. Yoo, K. Watanabe, T. Taniguchi, C. Nuckolls, P. Kim, J. Hone, *ACS Nano* **2013**, *7*, 7931.
[18] J. Scott Bunch, A. M. van der Zande, S. S. Verbridge, I. W. Frank, M. Tanenbaum, J. M. P. David, H. G. Craighead, P. L. McEuen, *Science* **2007**, *315*, 490.
[19] D. X. Luong, *Nature* **2020**, *577*, 647.
[20] P. Y. Huang, C. S. Ruiz-Vargas, A. M. Van Der Zande, W. S. Whitney, M. P. Levendorf, J. W. Kevek, S. Garg, J. S. Alden, C. J. Hustedt, Y. Zhu, J. Park, P. L. McEuen, D. A. Muller, *Nature* **2011**, *469*, 389.
[21] G. H. Lee, R. C. Cooper, S. J. An, S. Lee, A. Van Der Zande, N. Petrone, A. G. Hammerberg, C. Lee, B. Crawford, W. Oliver, J. W. Kysar, J. Hone, *Science* **2013**, *340*, 1073.
[22] S. Bertolazzi, J. Brivio, A. Kis, *ACS Nano* **2011**, *5*, 9703.
[23] C. Lee, X. Wei, J. W. Kysar, J. Hone, *Science* **2008**, *321*, 385.
[24] Y. Yang, X. Li, M. Wen, E. Hacopian, W. Chen, Y. Gong, J. Zhang, B. Li, W. Zhou, P. M. Ajayan, Q. Chen, T. Zhu, J. Lou, *Adv. Mater.* **2017**, *29*, 1604201.
[25] K. Kim, V. I. Artyukhov, W. Regan, Y. Liu, M. F. Crommie, B. I. Yakobson, A. Zettl, *Nano Lett.* **2012**, *12*, 293.
[26] S. Wang, Z. Qin, G. S. Jung, F. J. Martin-Martinez, K. Zhang, M. J. Buehler, J. H. Warner, *ACS Nano* **2016**, *10*, 9831.
[27] G. S. Jung, S. Wang, Z. Qin, F. J. Martin-Martinez, J. H. Warner, M. J. Buehler, *ACS Nano* **2018**, *12*, 3600.
[28] G. S. Jung, S. Wang, Z. Qin, S. Zhou, M. Danaie, A. I. Kirkland, M. J. Buehler, J. H. Warner, *ACS Nano* **2019**, *13*, 5693.
[29] T. H. Ly, J. Zhao, M. O. Cichocka, L.-J. Li, Y. H. Lee, *Nat. Commun.* **2017**, *8*, 14116.
[30] L. Huang, F. Zheng, Q. Deng, Q. H. Thi, L. W. Wong, Y. Cai, N. Wang, C. S. Lee, S. P. Lau, T. H. Ly, J. Zhao, *Sci. Adv.* **2020**, *6*, eabc2282.
[31] Y. Manzanares-Negro, G. López-Polín, K. Fujisawa, T. Zhang, F. Zhang, E. Kahn, N. Perea-López, M. Terrones, J. Gómez-Herrero, C. Gómez-Navarro, *ACS Nano* **2021**, *15*, 1210.
[32] A. Barreiro, F. Börrnert, M. H. Rümmeli, B. Büchner, L. M. K. Vandersypen, *Nano Lett.* **2012**, *12*, 1873.
[33] D. Kim, Y. Kim, J. Ihm, E. Yoon, G. Do Lee, *Carbon* **2015**, *84*, 146.
[34] Z. Song, V. I. Artyukhov, B. I. Yakobson, Z. Xu, *Nano Lett.* **2013**, *13*, 1829.
[35] Z. Zhang, A. Kutana, B. I. Yakobson, *Nanoscale* **2015**, *7*, 2716.
[36] S. S. Terdalkar, S. Huang, H. Yuan, J. J. Rencis, T. Zhu, S. Zhang, *Chem. Phys. Lett.* **2010**, *494*, 218.
[37] G. Jung, Z. Qin, M. J. Buehler, *Extreme Mech. Lett.* **2015**, *2*, 52.
[38] G. López-Polín, J. Gómez-Herrero, C. Gómez-Navarro, *Nano Lett.* **2015**, *15*, 2050.
[39] D. Wang, J. Zhao, S. Hu, X. Yin, S. Liang, Y. Liu, S. Deng, *Nano Lett.* **2007**, *7*, 1208.
[40] R. Fei, W. Li, J. Li, L. Yang, *Appl. Phys. Lett.* **2015**, *107*, 173104.
[41] H. L. Zhuang, M. D. Johannes, M. N. Blonsky, R. G. Hennig, *Appl. Phys. Lett.* **2014**, *104*, 022116.
[42] M. A. L. Marques, H. E. Troiani, M. Miki-Yoshida, M. Jose-Yacaman, A. Rubio, *Nano Lett.* **2004**, *4*, 811.
[43] C. Zhu, M. Yu, J. Zhou, Y. He, Q. Zeng, Y. Deng, S. Guo, M. Xu, J. Shi, W. Zhou, L. Sun, L. Wang, Z. Hu, Z. Zhang, W. Guo, Z. Liu, *Nat. Commun.* **2020**, *11*, 772.
[44] C. S. Ruiz-Vargas, H. L. Zhuang, P. Y. Huang, A. M. Van Der Zande, S. Garg, P. L. McEuen, D. A. Muller, R. G. Hennig, J. Park, *Nano Lett.* **2011**, *11*, 2259.
[45] T. Zhao, C. Xu, W. Ma, Z. Liu, T. Zhou, Z. Liu, S. Feng, M. Zhu, N. Kang, D. M. Sun, H. M. Cheng, W. Ren, *Nat. Commun.* **2019**, *10*, 4854.
[46] R. Grantab, V. B. Shenoy, R. S. Ruoff, *Science* **2010**, *330*, 946.
[47] Y. C. Lin, H. P. Komsa, C. H. Yeh, T. Björkman, Z. Y. Liang, C. H. Ho, Y. S. Huang, P. W. Chiu, A. V. Krasheninnikov, K. Suenaga, *ACS Nano* **2015**, *9*, 11249.
[48] L. Hart, S. Dale, S. Hoye, J. L. Webb, D. Wolverson, *Nano Lett.* **2016**, *16*, 1381.
[49] E. Liu, Y. Fu, Y. Wang, Y. Feng, H. Liu, X. Wan, W. Zhou, B. Wang, L. Shao, C. H. Ho, Y. S. Huang, Z. Cao, L. Wang, A. Li, J. Zeng, F. Song, X. Wang, Y. Shi, H. Yuan, H. Y. Hwang, Y. Cui, F. Miao, D. Xing, *Nat. Commun.* **2015**, *6*, 6991.
[50] S. Tongay, H. Sahin, C. Ko, A. Luce, W. Fan, K. Liu, J. Zhou, Y. S. Huang, C. H. Ho, J. Yan, D. F. Ogletree, S. Aloni, J. Ji, S. Li, J. Li, F. M. Peeters, J. Wu, *Nat. Commun.* **2014**, *5*, 3252.
[51] X. Li, X. Wang, J. Hong, D. Liu, Q. Feng, Z. Lei, K. Liu, F. Ding, H. Xu, *Adv. Funct. Mater.* **2019**, *29*, 1906385.
[52] H. Wang, E. Liu, Y. Wang, B. Wan, C. H. Ho, F. Miao, X. G. Wan, *Phys. Rev. B* **2017**, *96*, 165418.
[53] X. Li, F. Cui, Q. Feng, G. Wang, X. Xu, J. Wu, N. Mao, X. Liang, Z. Zhang, J. Zhang, H. Xu, *Nanoscale* **2016**, *8*, 18956.
[54] H. Li, S. Wang, T. Samuels, G. Ggoch, D. Han, C. S. Allen, A. I. Kirkland, J. C. Grossman, H. Jamie, *ACS Nano* **2017**, *11*, 3392.
[55] G. Kresse, J. Furthmüller, *Phys. Rev. B* **1996**, *54*, 11169.
[56] J. P. Perdew, K. Burke, M. Ernzerhof, *Phys. Rev. Lett.* **1996**, *77*, 3865.
[57] J. P. Perdew, Y. Wang, *Phys. Rev. B* **2018**, *98*, 244.